PHYSICAL REVIEW B **88**, 214115 (2013)

Control of oxygen octahedral rotations and physical properties in $SrRuO_3$ films

Wenlai Lu,[1,2] Ping Yang,[3] Wen Dong Song,[2] Gan Moog Chow,[1] and Jing Sheng Chen[1,*]
[1]*Department of Materials Science and Engineering, National University of Singapore, Singapore 117576, Singapore*
[2]*Data Storage Institute, A*STAR (Agency for Science, Technology and Research), DSI Building, 5 Engineering Drive 1, Singapore 117608, Singapore*
[3]*Singapore Synchrotron Light Source (SSLS), National University of Singapore, 5 Research Link, Singapore 117603, Singapore*

(Received 13 October 2013; revised manuscript received 2 December 2013; published 30 December 2013)

Control of octahedral rotations in the ABO_3 perovskite oxides has been of great interest due to its potential in rationally discovering and designing new multifunctional phases. In this study, we show that octahedral rotations of the $SrRuO_3$ films can be controlled by oxygen vacancies as well as by interfacial coupling, which further determines the physical properties. Half-integer reflections using high-resolution synchrotron x-ray diffraction were carried out to determine the octahedral rotation pattern of $SrRuO_3$ films on $SrTiO_3$ substrates. The transition of RuO_6 rotation pattern accompanied by the structural change from monoclinic $P2_1/m$ to tetragonal $F4/mmc$ can be understood from the preference of oxygen vacancies in the SrO atomic plane and the coupling of octahedra across the interface between film and substrate. The field angle dependence of magnetoresistance further confirmed the structural phase transition with changes in octahedral rotations. The monoclinic phase has the uniaxial magnetic easy axis 30° away from the [001] direction towards the [010] direction while the tetragonal phase has uniaxial magnetic easy axis along the fourfold axis which is perpendicular to the film surface. This study demonstrates the ability to control the octahedral rotations in perovskite films and its importance when designing thin films and multilayers with desired functional property.

DOI: 10.1103/PhysRevB.88.214115 PACS number(s): 61.05.cp, 68.55.−a, 77.80.bn

I. INTRODUCTION

Transition metal oxides of the ABO_3 perovskite class have attracted broad interest due to their intriguing physical properties such as colossal magnetoresistance, superconductivity, charge ordering, as well as their potential applications in low-power electronics, energy storage, and conversion.[1–4] The strong electron-lattice correlations present in the perovskite-type materials lead to an even broader range of functionalities realized by lattice distortions.[5–13] A lower symmetry than the ideal cubic structure should result from this lattice distortion, which is common in perovskite materials and associated with either Jahn-Teller distortion (e.g. $LaMnO_3$), cation displacement (e.g. $BaTiO_3$), or rotations of rigid octahedra ($CaTiO_3$, $SrRuO_3$, $LaAlO_3$, etc.). Particularly, the ubiquitous rotation of corner-sharing BO_6 octahedra in perovskites modifies the B-O-B bond angles and critically affects the material properties. For example, a nonpolar $BiFeO_3$ phase has been stabilized with changes in octahedral rotations across the interface.[14] Octahedral rotations in $EuZrO_3$ and $EuHfO_3$ also enhance the superexchange interactions whereby the magnetic ground state can be switched from ferromagnetism to antiferromagnetism.[15] Recently, a rotation-driven ferroelectricity has been experimentally observed[16] and theoretically predicted[17] in artificial perovskite superlattices. This discovery has inspired the search for a novel mechanism mediated by octahedral rotations in pursuit of new functionalities. Rotomagnetism is one such example in which the magnetic order is induced by octahedral rotations.[18] Furthermore, a path to pursue strong magnetoelectric coupling has been suggested by actively utilizing the octahedral rotations.[19] Control of oxygen octahedral rotations is therefore a powerful approach to engineer the electronic and ferroic behaviors and to design novel multifunctional materials.

In spite of the recognized importance of octahedral rotations to properties of thin films, rational control over functionalities via octahedral rotations is still rare experimentally.[14,16] This is in part due to the difficulties in obtaining oxygen positions with high precision that are crucial in determining the patterns and magnitudes of octahedral rotations. In perovskites, the BO_6 corner-shared structure has long been defined and classified into different tilt systems, which describe the patterns and magnitudes of octahedral rotations about the three pseudocubic axes.[20] The magnitudes of the rotations are indicated by a set of three letters which refer to the axes in the order [100], [010], [001], and the sense of the rotations are denoted by the superscripts $+$, $-$, or 0 to show whether the successive octahedra about that particular axis are rotated in phase, out of phase, or have no rotations. Although the method to determine the octahedral tilt system has been suggested and was successfully applied to bulk perovskites in the 1970s,[21] the octahedral rotations in epitaxial thin films have been poorly understood and rarely characterized owing to the limited sample volume and the weak scattering from oxygen atoms. Both extended x-ray absorption fine structure and multiple-diffraction rod analysis techniques have been utilized to investigate the octahedral rotations in perovskite films; however, the complexity of the data analysis has limited their extensive use.[22,23] Recently, advances in transmission electron microscopy and high-flux synchrotron x-ray sources have enabled the measurements of the rotation patterns and magnitudes of octahedral tilts in thin perovskite films.[24–30] This development in experimental techniques dramatically simplifies the data analysis process and permits the understanding of geometric rotation patterns of octahedra in thin film perovskites.

To realize a new phase with different properties by control over the octahedral framework, we focus on a nearly half-metallic material $SrRuO_3$ (SRO) with strong hybridization between Ru 4*d* and O 2*p* orbitals, whose electronic structure is significantly affected by the rotation of the rigid RuO_6 octahedra.[31] In bulk SRO, the octahedral tilt system transits from $\mathbf{a^+c^-c^-}$ to $\mathbf{a^0a^0c^-}$ at 820 K with a structural phase transition from orthorhombic to tetragonal structure.[32] In epitaxial SRO films, on the other hand, versatile structural symmetries have been reported, which may correspond to different octahedral tilt systems.[33–37] However, the octahedral rotation pattern was poorly understood or was only inferred from the lattice parameters measurements.[33,36,37] Therefore, direct measurement of octahedral tilts by half-integer reflections using synchrotron x-ray is essential for a complete determination of rotation pattern of the corner-connected RuO_6 blocks.

In this paper, we report the stabilization of nonequilibrium rotation pattern of $\mathbf{a^0a^0c^-}$ in SRO films on $SrTiO_3$ (STO) substrate through the intentional introduction of oxygen vacancies and the interfacial coupling of the film's octahedra with that of the substrate. The octahedral tilt system transits from $\mathbf{a^-b^+c^-}$ to $\mathbf{a^0a^0c^-}$, concomitant with the monoclinic to tetragonal structural phase transition. Half-integer reflections were utilized to determine the octahedral tilt system. We observed that increasing film thickness and oxygen partial pressure stabilized the monoclinic phase with $\mathbf{a^-b^+c^-}$ tilt, whereas decreasing film thickness and oxygen partial pressure resulted in the tetragonal phase with $\mathbf{a^0a^0c^-}$ tilt. Physical properties further confirmed the monoclinic-to-tetragonal phase transition. The monoclinic phase has an easy axis between [001] and [100] directions, while the tetragonal phase has the uniaxial magnetic easy direction along the fourfold axis normal to the film plane. In addition, the monoclinic phase has diverse magnetoresistance (MR) along the two orthogonal in-plane directions, while the tetragonal phase exhibits the same in-plane MR. The results highlight the ability to control the octahedral rotations and physical properties in perovskite oxide films via oxygen vacancies and interfacial coupling, which is a promising strategy to further expand the functionalities in perovskites.

II. EXPERIMENT

Epitaxial SRO $(001)_{pc}$ films were deposited on STO (001) substrates by pulsed laser deposition (PLD) with KrF excimer laser ($\lambda = 248$ nm, 2 Hz) pulses of 250 mJ focused on stoichiometric ceramic SRO target. The substrate to target distance was kept at 60 mm. The substrate temperature was fixed at 450 °C, measured by a double-wavelength pyrometer. The oxygen content was controlled by varying the oxygen partial pressure from 100 to 30 mTorr during the deposition, and the different oxygen content was confirmed by x-ray photoelectron spectroscopy (XPS). After the deposition, all the films were cooled down to room temperature at 20 K/min under the oxygen pressure of 100 mTorr. The film thickness was calculated from Laue oscillation intervals that can be observed in $(00L)$ scans.

The crystal structures and the octahedral rotation patterns of the monoclinic and tetragonal SRO film were determined by high-resolution x-ray diffractometer using synchrotron x-ray sources at the x-ray development and demonstration (XDD) beam line of Singapore Synchrotron Light Source (SSLS) and Shanghai Synchrotron Radiation Facility (SSRF). The octahedral rotation patterns were determined from a set of L scans including $(^1/_2\ 0\ L)$, $(0\ ^1/_2\ \mathrm{L})$, $(^1/_2\ ^1/_2\ L)$, and $(^1/_2\ ^3/_2\ L)$.

The magnetic properties were investigated by a superconducting quantum interference device (SQUID). The temperature dependence of magnetization was measured after field-cooled from room temperature with the application of a 100 Oe magnetic field. Magnetizations along different crystal orientations were measured.

The magnetoresistance was measured by a linear array 4-point probes method using a Physical Property Measurement System (PPMS; Quantum Design) equipped with a sample rotator. During the measurement, the temperature was kept at 2 K, and the samples were rotated under the application of a 4 Tesla magnetic field so that the field angle dependence of magnetoresistance can be obtained. The currents were kept perpendicular to the magnetic field all through the measurement.

III. RESULTS AND DISCUSSION

A. Crystal structures

The SRO thin films were grown under oxygen partial pressures of 30, 60, and 100 mTorr, respectively, on $SrTiO_3$ (STO) (001) substrates. The film thickness was varied from 6 to 80 nm. The presence of oxygen vacancies in films fabricated under reduced oxygen partial pressure was confirmed from the depth profile using x-ray photoelectron spectroscopy and was reported elsewhere.[38] X-ray diffraction (XRD) θ-2θ scans show only the $00l$ peaks from SRO film and STO substrate, confirming the epitaxial growth of the films. In Fig. 1(a), the presence of Laue oscillations around the SRO 002 peak ensures the good crystallinity and smooth surfaces (or interfaces) of both oxygen sufficient and deficient film. Similarly, Laue oscillations are also observed in films with different thicknesses [Fig. 1(b)]. These clear oscillations around the SRO 002 peaks were used to calculate the film thickness using the following equation:

$$t = a_{\mathrm{STO}}/\Delta L, \tag{1}$$

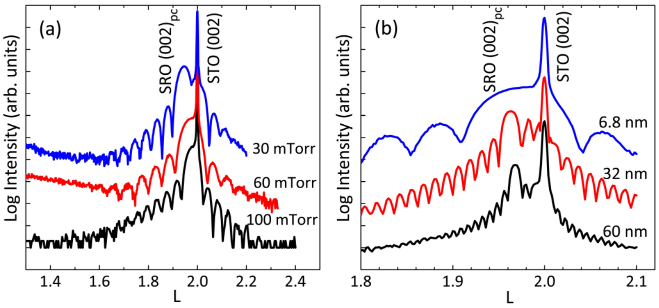

FIG. 1. (Color online) (a) X-ray diffraction pattern of ~10 nm SRO thin films deposited on STO under various oxygen partial pressures. (b) X-ray diffraction pattern of SRO films grown in 60 mTorr oxygen with different thicknesses. Subscript *pc* stands for pseudocubic unit cell.

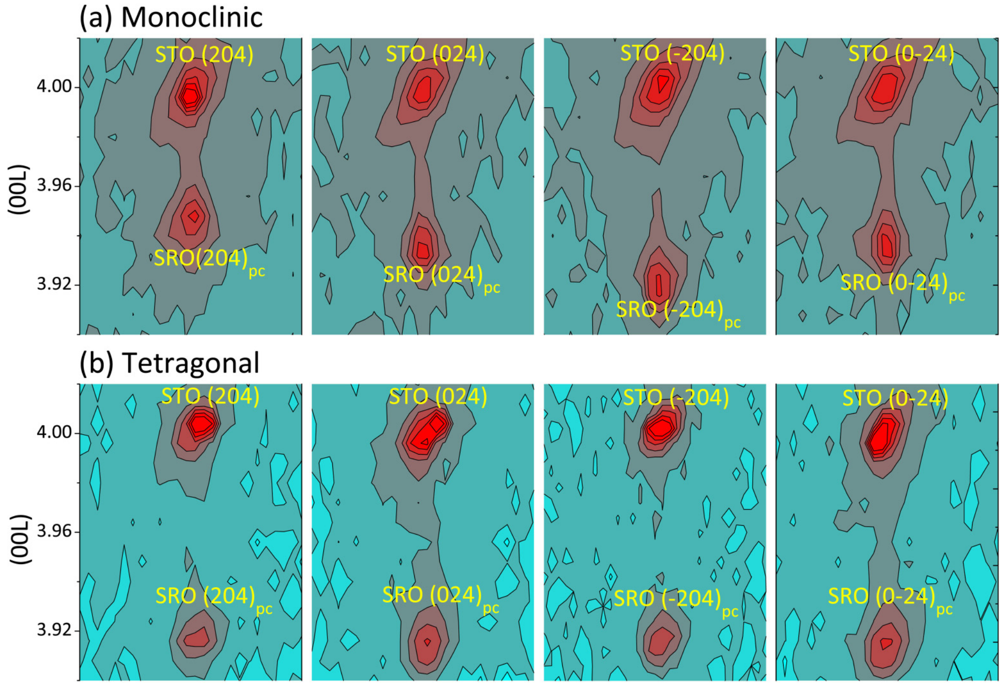

FIG. 2. (Color online) Reciprocal space mappings around STO {204}. (a) Monoclinic film deposited in 60 mTorr oxygen and with a thickness of 60 nm, (b) tetragonal film grown in 30 mTorr oxygen and with a thickness of 80 nm.

where t is the film thickness, a_{STO} is the lattice constant of the STO substrate and ΔL is the interval between the two neighboring oscillations. The shift of SRO 002 peak towards lower L value indicates that the out-of-plane lattice spacing d_{001} increases with either decreasing oxygen partial pressure or film thickness, implying that the crystal structure is highly dependent on both the oxygen content and film thickness.

The crystal structure of the SRO film was examined by reciprocal space mappings (RSMs) using high-resolution XRD (HR-XRD) around {204} STO Bragg reflections. All the SRO films are completely strained on the STO substrates, inferred from the vertical alignment of the SRO and STO reciprocal lattice point. Consider the position of the SRO reciprocal lattice point in the {204} mappings. In Fig. 2(a), the different L values of SRO (204) and SRO (−204) indicate an oblique angle between the reciprocal lattice vectors **H** and **L**, and thus the angle β between direct lattice vectors $\boldsymbol{a}$ and $\boldsymbol{c}$ is unequal to 90°. On the other hand, the same L values of SRO (024) and SRO (0-24) indicate a 90° angle between vectors $\boldsymbol{b}$ and $\boldsymbol{c}$ in the direct lattice. That means $\alpha = 90°$. The relationship between the reciprocal lattice points and the unit cell angles are graphically shown in the Appendix, Fig. 9. Based on this established principle, we are able to identify the crystal system of SRO film from the L values in the $(0 \pm KL)$ and $(\pm H0L)$ mappings. With varied thickness and oxygen partial pressure, there are two kinds of structures formed: one is the usually reported monoclinic structure represented by the dissimilar L values [Fig. 2(a)] in the {204} mappings; the other is the tetragonal structure indicated by the same L value [Fig. 2(b)] in the {204} mappings. The exact lattice parameters can be calculated from the position of SRO (002), (-103), and (013) reciprocal lattice point in the reciprocal space of STO. For the 60 nm film deposited in 60 mTorr oxygen, it exhibits a monoclinic unit cell with $a_{pc} = 3.905$ (±0.004), $b_{pc} = 3.905$ (±0.004), $c_{pc} = 3.970$ (±0.002), $\alpha = 90.0$ (±0.1)°, $\beta = 89.6$ (±0.1)°, $\gamma = 90.0$ (±0.1)°. On the other hand, for the tetragonal SRO film with a thickness of 80 nm and fabricated in 30 mTorr oxygen, we have a unit cell with $a_{pc} = 3.905$ (±0.004), $b_{pc} = 3.905$ (±0.004), $c_{pc} = 4.026$ (±0.002), $\alpha = 90.1$ (±0.1)°, $\beta = 90.0$ (±0.1)°, $\gamma = 89.9$ (±0.1)°. Ultrathin (<10 nm) film grown in oxygen partial pressure lower than 60 mTorr exhibits the same tetragonal structural symmetry.

B. Octahedral rotations identification by half-integer reflection

Half-integer reflections are required in order to confirm the octahedral rotation pattern of the monoclinic SRO phase and to identify the rotation pattern of the tetragonal phase. According to Glazer,[21] half-integer reflections are produced as a consequence of the tilting of the octahedra. These reflections can be indexed with some indices of hkl odd, and the ordinary reflections (main reflections) are indexed with all hkl even on the doubled cell $2a_{pc} \times 2b_{pc} \times 2c_{pc}$. The in-phase (**+**) and out-of-phase (**−**) tilts can be distinguished easily: ½ odd-odd-even type of reflections are produced by **+** tilts, while ½ odd-odd-odd reflections are produced by **−** tilts. The relationship between the type of tilt (+ or −) and the measured half-integer reflections are summarized in Table I.[21]

Based on a set of L scans for $({}^{1}/_{2}\ 0\ L)$, $(0\ {}^{1}/_{2}\ L)$, $({}^{1}/_{2}\ {}^{1}/_{2}\ L)$, and $({}^{1}/_{2}\ {}^{3}/_{2}\ L)$, we are able to determine the octahedral rotation pattern and thus the space group of the SRO film (note that the number of measured reflections were limited by the experimental setup of the four-circle diffractometer from the geometrical consideration). In Fig. 3(a), the 60 nm film deposited in 60 mTorr oxygen (it exhibits monoclinic structure determined from the lattice parameter measurements) shows

TABLE I. Half-integer reflections corresponding to different types of octahedral tilt.[21]

Type of tilt	Half-integer reflection	Restrictions	Examples
$\mathbf{a}^+$	${}^1/_2$ even-odd-odd	$k \neq l$	$0\,{}^1/_2\,{}^3/_2$, $0\,{}^1/_2\,{}^5/_2$
$\mathbf{b}^+$	${}^1/_2$ odd-even-odd	$h \neq l$	${}^1/_2\,0\,{}^3/_2$, ${}^1/_2\,0\,{}^5/_2$
$\mathbf{c}^+$	${}^1/_2$ odd-odd-even	$h \neq k$	${}^1/_2\,{}^3/_2\,1$, ${}^1/_2\,{}^3/_2\,2$
$\mathbf{a}^-$	${}^1/_2$ odd-odd-odd	$k \neq l$	${}^1/_2\,{}^1/_2\,{}^3/_2$, ${}^3/_2\,{}^1/_2\,{}^3/_2$
$\mathbf{b}^-$	${}^1/_2$ odd-odd-odd	$h \neq l$	${}^1/_2\,{}^1/_2\,{}^3/_2$, ${}^1/_2\,{}^3/_2\,{}^3/_2$
$\mathbf{c}^-$	${}^1/_2$ odd-odd-odd	$h \neq k$	${}^3/_2\,{}^1/_2\,{}^3/_2$, ${}^1/_2\,{}^3/_2\,{}^3/_2$

the following half-integer reflections ${}^1/_2\,0\,{}^3/_2$, ${}^1/_2\,0\,{}^5/_2$, ${}^1/_2\,{}^1/_2\,{}^3/_2$, ${}^1/_2\,{}^1/_2\,{}^5/_2$, ${}^1/_2\,{}^3/_2\,{}^3/_2$, and ${}^1/_2\,{}^3/_2\,{}^5/_2$. From the presence or absence of the half-integer reflections, we are able to determine the rotation pattern step by step based on Table I.

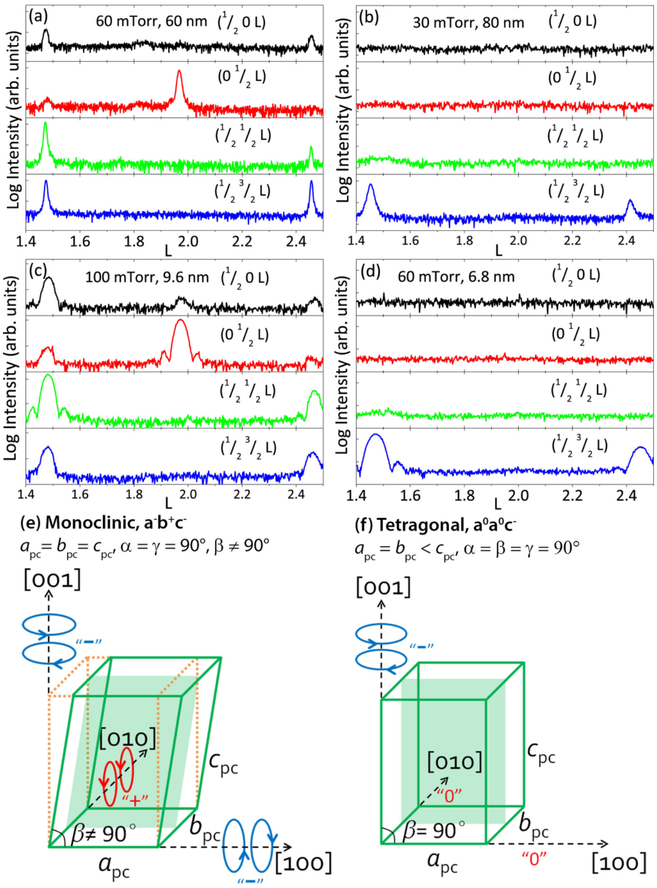

FIG. 3. (Color online) Half-integer reflections of SRO films for monoclinic phase, (a) deposited in 60 mTorr and with a thickness of 60 nm, (c) deposited in 100 mTorr with 9.6 nm thickness; and tetragonal phase, (b) deposited in 30 mTorr and with a thickness of 80 nm, (d) deposited in 60 mTorr with 6.8 nm thickness. The schematic drawing of the pseudocubic unit cell and rotation pattern of (e) monoclinic phase with $\mathbf{a}^-\mathbf{b}^+\mathbf{c}^-$ tilt system and (f) tetragonal phase with $\mathbf{a}^0\mathbf{a}^0\mathbf{c}^-$ tilt system is clearly shown. The out-of-phase octahedral tilts are indicated by blue circles, while the in-phase tilts are represented by red circles. The absence of tilts is indicated by red "0".

Firstly, $\mathbf{b}^+$ tilt is indicated by the presence of ${}^1/_2\,0\,{}^3/_2$ and ${}^1/_2\,0\,{}^5/_2$ peaks, and this rules out the possibility of $\mathbf{b}^-$ tilt. Secondly, $\mathbf{a}^-$ tilt is suggested from the ${}^1/_2\,{}^1/_2\,{}^3/_2$ and ${}^1/_2\,{}^1/_2\,{}^5/_2$ peaks considering the absence of $\mathbf{b}^-$ tilt. Finally, the presence of ${}^1/_2\,{}^3/_2\,{}^3/_2$ peak indicates the existence of $\mathbf{c}^-$ tilt, and the absence of ${}^1/_2\,{}^3/_2\,2$ peak excludes the possibility of $\mathbf{c}^+$ tilt. Note that $0\,{}^1/_2\,1$ peak, which arises from the doubling of lattice along the b axis, is produced by $\mathbf{b}^+$ tilt.[27] From these reflections, the rotation pattern for the monoclinic structure can be easily inferred to be $\mathbf{a}^-\mathbf{b}^+\mathbf{c}^-$ if only considering the sense of rotation, with out-of-phase tilts about the a and c axes and in-phase tilts about the b axis. It is of interest to examine if this tilt system may be further simplified by considering the magnitude of rotations. In bulk SRO with rigid octahedra, the equality of any two tilt angles results in the same unit cell length along those two particular axes due to the nearly uniform bond lengths. In strained SRO films however, both octahedral distortions and rotations are present to accommodate the epitaxial strain.[39] Therefore, the same lattice parameters a_{pc} and b_{pc} of the monoclinic structure (inferred from the same horizontal position of SRO and STO in {204} mappings) do not necessarily indicate the equal magnitude of the tilts about the a and b axes. The tilt system of the monoclinic phase is thus $\mathbf{a}^-\mathbf{b}^+\mathbf{c}^-$ rather than $\mathbf{a}^-\mathbf{a}^+\mathbf{c}^-$, with a space group $P2_1/m$. Note that there is a weak $0\,{}^1/_2\,{}^3/_2$ peak as shown in the red curve in Fig. 3(a), indicating the presence of + tilt about [100] direction. This is probably due to the existence of a minor domain with $a^+b^-c^-$ tilt that is essentially the same but is perpendicular to the major domain. The mixture of $a^-b^+c^-$ and $a^+b^-c^-$ domains is more noticeable for the 100 mTorr, 9.6 nm film as shown in Fig. 3(c). There is a strong ${}^1/_2\,0\,{}^3/_2$ peak corresponding to in-phase (+) tilt about [010] axis, and there is also a weak $0\,{}^1/_2\,{}^3/_2$ peak corresponding to in-phase (+) tilt about [100] axis. This indicates the coexistence of the major domain with $a^-b^+c^-$ tilt and the minor domain with $a^+b^-c^-$ tilt in this monoclinic thin film. The schematic diagram of the RuO_6 octahedral rotations of this monoclinic unit cell is shown in Fig. 3(e) (blue circles represent out-of-phase rotations, while red circles represent in-phase rotations). The signs of the tilts are important for determining the unit-cell angles. According to Glazer,[21] any two **−** tilts indicate that the two relevant axes are inclined to each other, while any two **+** (or **0**) tilts, or one **+** (or **0**) and one **−** tilt, mean that the relevant cell axes are normal to each other. Thus, $\mathbf{a}^-\mathbf{b}^+\mathbf{c}^-$ has the b axis normal to the other two axes, while the a axis is inclined to c, meaning that the angle β between a and c is unequal to 90°, which is consistent with the unit-cell angles determined from the lattice parameter measurements mentioned above.

For the 80 nm film deposited in 30 mTorr oxygen and ultrathin (<10 nm) film deposited in lower-than-60 mTorr oxygen (both of them have tetragonal structure according to lattice parameter measurements), only half-integer reflections of ${}^1/_2\,{}^3/_2\,{}^3/_2$ and ${}^1/_2\,{}^3/_2\,{}^5/_2$ are observed as displayed in Figs. 3(b) and 3(d). The absence of $0\,{}^1/_2\,{}^3/_2$, ${}^1/_2\,0\,{}^3/_2$, and ${}^1/_2\,{}^1/_2\,{}^3/_2$ reflections implies that neither **+** tilts nor **−** tilts exist about the in-plane axes a and b, denoted by superscript "0" appropriate to the relevant axes. In addition, since the ${}^1/_2\,{}^3/_2\,2$ reflection is absent and the observed reflections of ${}^1/_2\,{}^3/_2\,{}^3/_2$ and ${}^1/_2\,{}^3/_2\,{}^5/_2$ are of the odd-odd-odd type, the tilt system $\mathbf{a}^0\mathbf{a}^0\mathbf{c}^-$ is immediately suggested. The tetragonal unit cell with

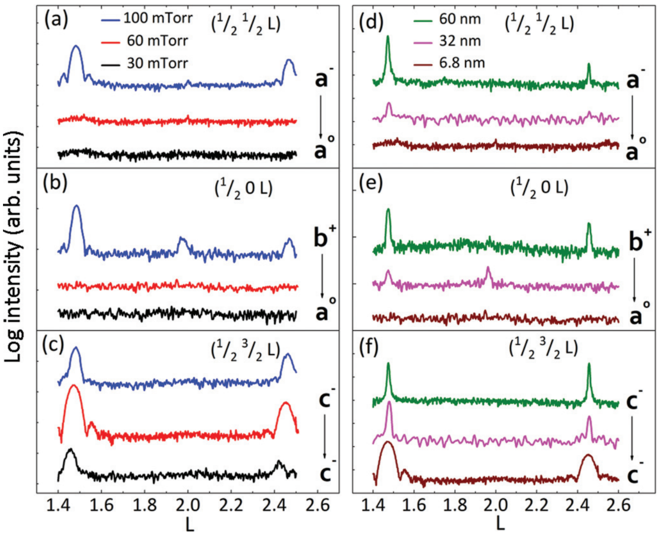

FIG. 4. (Color online) Half-integer reflections for (a)–(c) SRO films with ~10 nm thickness and varied oxygen content, and (d)–(f) SRO films with same oxygen content and different thicknesses. The observed half-integer peaks arise from (a), (d) $\mathbf{a}^-$ tilts about [100] axis, (b), (e) $\mathbf{b}^-$ tilts about [010] axis, and (c), (f) $\mathbf{c}^-$ tilts about [001] axis. Both ($^1/_2$ $^1/_2$ L) and ($^1/_2$ 0 L) L scans exhibit reduced intensity of the half-integer peaks with decreasing the oxygen partial pressure or film thickness, indicating the suppressed octahedral tilts about [100] and [010] axes.

such rotation pattern is clearly illustrated in Fig. 3(f), with no tilts about the two in-plane axes and out-of-phase rotations about the [001] axis. The two equal in-plane lattice parameters a_{pc} and b_{pc} are normal to each other and are both normal to c_{pc} inferred from the signs of "**0**" and "**–**". The space group of this tilt is $F4/mmc$ and, being tetragonal, is in agreement with the measured unit-cell geometry.

C. Control of octahedral rotations

In order to control the rotations of octahedra in SRO films, we studied the effect of oxygen partial pressure and film thickness on the octahedral rotations. Half-integer L scans of ($^1/_2$ $^1/_2$ L), ($^1/_2$ 0 L), and ($^1/_2$ $^3/_2$ L) are utilized to investigate the rotations about the a, b, and c axis, respectively. In our cases, $^1/_2$ $^1/_2$ $^3/_2$ reflections are produced by $\mathbf{a}^-$ tilt, while $\mathbf{b}^+$ tilt and $\mathbf{c}^-$ tilt give rise to $^1/_2$ 0 $^3/_2$ and $^1/_2$ $^3/_2$ $^3/_2$ peaks, respectively. In Figs. 4(a)–4(c), all the films have a thickness of ~10 nm. The $^1/_2$ $^3/_2$ $^3/_2$ reflection appears in samples deposited in different oxygen partial pressures, indicating that the $\mathbf{c}^-$ tilts are present in all SRO films. In contrast, the reflections $^1/_2$ 0 $^3/_2$ and $^1/_2$ $^1/_2$ $^3/_2$ are only observed in samples grown in 100 mTorr oxygen, suggesting that the $\mathbf{b}^+$ and $\mathbf{a}^-$ tilts only persist in high-pressure-grown monoclinic samples, whereas they are forbidden in oxygen-deficient films that are tetragonal. Therefore, it can be concluded that, by reducing the oxygen content in SRO film, the octahedral rotations around in-plane axes are suppressed, while the tilts about the out-of-plane axis are sustained.

Similar to the effect of oxygen content, film thickness also plays a crucial role in determining the octahedral rotations. Figures 4(d)–4(f) show the thickness-dependent octahedral rotations around the in-plane and out-of-plane directions, respectively. All the films were deposited at the same oxygen partial pressure of 60 mTorr. It is shown in Fig. 4(f) that the octahedral rotations around the out-of-plane direction, represented by $^1/_2$ $^3/_2$ $^3/_2$ reflections, persist in all samples regardless of the film thickness. However, the $^1/_2$ $^1/_2$ $^3/_2$ peak gradually disappears with the decrease in film thickness [in Fig. 4(d)], indicating that the octahedral rotations along the a axis are gradually diminished, possibly due to the enhanced interfacial coupling of octahedral rotations in ultrathin films (as discussed below). The $\mathbf{b}^+$ tilt along the b axis, demonstrated by the $^1/_2$ 0 $^3/_2$ peak in Fig. 4(e), also shows similar suppression by reducing the film thickness.

In order to have an overall understanding of the structural phase transition with varied oxygen content and film thickness, we show the evolution of octahedral tilts in a single figure, demonstrated by the intensity variation of half-integer reflections. However, the absolute intensities of the half-integer reflections are dramatically different if measured at different times of the day, since the beam current may decay from 200–300 mA during the daytime to less than 100 mA at night in the decay operation mode. Therefore, we used ratios of $I_{1/2(113)}/I_{1/2(133)}$ and $I_{1/2(103)}/I_{1/2(133)}$ instead of the absolute intensity values to reveal the evolution of octahedral tilts. The values of these two indices are displayed in colors generated by interpolation from blue to magenta. Blue represents the absence of tilts about in-plane axes, while magenta suggests the persistence of octahedral tilts about in-plane direction. As illustrated in Figs. 5(a) and 5(b), the octahedral tilts along in-plane axes ($\mathbf{a}^-$ and $\mathbf{b}^+$) versus along the out-of-plane axis ($\mathbf{c}^-$) are significantly suppressed with the combined effects of decreasing the film thickness and reducing the oxygen partial pressure. The transition of octahedral rotation pattern from $\mathbf{a}^-\mathbf{b}^+\mathbf{c}^-$ to $\mathbf{a}^0\mathbf{a}^0\mathbf{c}^-$ tilt is indicated by a dotted line, implying the phase transition from monoclinic to tetragonal structure, as reflected by the color conversion from magenta to blue.

The phase transition between $\mathbf{a}^-\mathbf{b}^+\mathbf{c}^-$ and $\mathbf{a}^0\mathbf{a}^0\mathbf{c}^-$ tilts in SRO film can be understood as follows. In our stoichiometric SRO films without oxygen vacancy, the octahedral tilts along each axis persist, resulting in a rotation pattern of $\mathbf{a}^-\mathbf{b}^+\mathbf{c}^-$ as is observed in the films grown at 100 mTorr. With decreasing oxygen partial pressure, oxygen vacancies are introduced in SRO films. While the ordering of oxygen vacancies in perovskite films is largely dependent on the strain state,[40–42] the oxygen vacancies in our grown SRO films on STO substrate prefer to reside in the SrO atomic plane rather than the RuO_2 plane.[37] Therefore, the octahedral tilts in the equatorial plane [shown in Fig. 6(a)] are hardly changed, while the tilts in the apical plane [shown in Fig. 6(b)] are dramatically affected. The missing oxygen ions at the octahedral apex [see Fig. 6(b)] increase the Ru-Ru repulsion along the c axis, which results in suppressed or even absent rotations of octahedra about the a and b axes. This explains the transition from $\mathbf{a}^-\mathbf{b}^+\mathbf{c}^-$ tilt to $\mathbf{a}^0\mathbf{a}^0\mathbf{c}^-$ tilt with decreasing the oxygen partial pressure. In addition to the oxygen vacancy, it has been shown both experimentally[26,43–45] and theoretically[31] that the structural coupling across hetero-interfaces also has profound influence on the octahedral tilts. The coupling of octahedra across the interface between the film and substrate is schematically

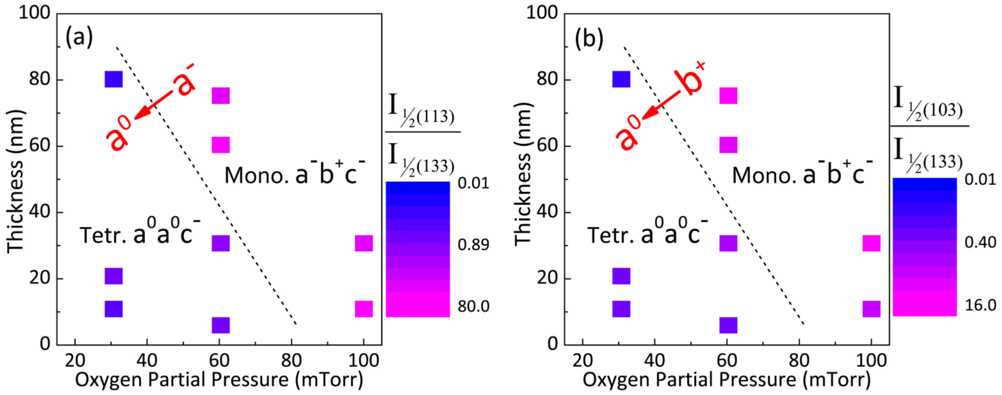

FIG. 5. (Color online) Evolution of the octahedral tilts with oxygen partial pressure and film thickness. (a) The octahedral rotations about [100] axis transit from out-of-phase (denoted by a^-) for monoclinic phase to no rotation (denoted by a^0) for tetragonal phase with the reduction in oxygen content and film thickness. (b) The octahedral rotations about [010] axis change from in-phase (denoted by b^+) for monoclinic phase to no rotation (denoted by a^0) for tetragonal phase with the decrease in oxygen content and film thickness. The ratios of $I_{1/2(113)}/I_{1/2(133)}$ and $I_{1/2(103)}/I_{1/2(133)}$, were used to follow this tilt transition, as reflected by the color conversion from magenta to blue.

shown in Figs. 6(c) and 6(d). The corner connectivity of the BO_6 octahedra enables the tilts in the substrate to be transferred across the interface and to propagate into the film. For the STO substrate that exhibits $\mathbf{a^0a^0a^0}$ tilt, the interfacial coupling imposes a force that tends to suppress the octahedral tilts about the *a* and *b* axes in SRO film. The degree of freedom remaining is then the octahedral tilt along the *c* axis. Therefore, $\mathbf{a^0a^0c^-}$ tilt is stabilized in thinner films, where the interfacial coupling becomes more dominant.

D. Control of physical properties

In the following, we show how the physical properties are coupled to the dramatically different octahedral rotation patterns present in the monoclinic and tetragonal phases, respectively. Figure 7 shows the temperature dependence of the magnetization curves of monoclinic and tetragonal films, which are thick or thin, oxygen deficient or sufficient. We find that all the monoclinic films have in-plane uniaxial anisotropy possibly resulting from the different rotation patterns about the *a* and *b* axes [Figs. 7(a) and 7(b)]. This in-plane anisotropy is in agreement with the previous results[46] and can be easily understood from the rotation pattern that the opposite sign of tilts in monoclinic phases breaks the symmetry along the orthogonal in-plane directions, while the octahedra rotate in-phase about the magnetically hard direction [010]. Note that the magnetization along the hard axis [010] in Fig. 7(b) slightly increases compared to that in Fig. 7(a). This is possibly due to the presence of a minor domain with $\mathbf{a^+b^-c^-}$ tilt that is essentially the same with the major domain ($\mathbf{a^-b^+c^-}$ tilt) but is different in orientation. The coexistence of these two domains finds evidence in Fig. 3(c). The stronger $^1/_2\,0\,^3/_2$ peak indicates the presence of + tilt about [010] axis appropriate to the major domain, while the weaker $0\,^1/_2\,^3/_2$ peak suggests the existence of + tilt about [100] axis that corresponds to the minor domain. For the tetragonal SRO phases, on the other hand, we observed a uniaxial magnetic easy axis along the film normal direction [Figs. 7(c) and 7(d)]. This perpendicular magnetic anisotropy observed in the tetragonal phase is closely related to the octahedral tilt system $\mathbf{a^0a^0c^-}$ and can be readily interpreted by the same octahedral tilts about in-plane axes and the only sustained octahedral rotations about the *c* axis, as illustrated in Fig. 3(f).

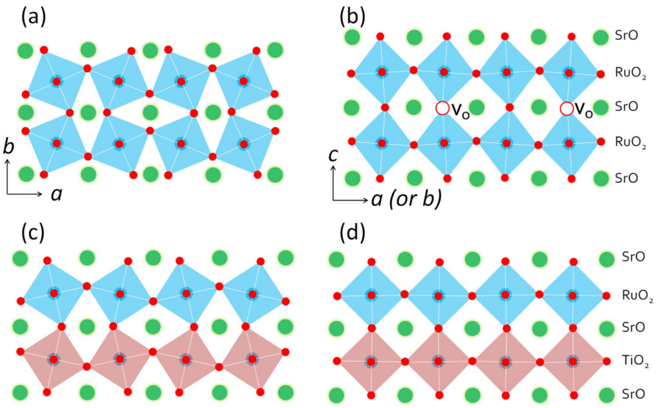

FIG. 6. (Color online) Effects of oxygen vacancies on octahedral tilts in the (a) equatorial plane and (b) apical plane in SRO films. (a) Octahedral tilts about *c* axis are sustained, while (b) the preference of oxygen vacancy (V_O) in the SrO atomic plane results in a suppressed octahedral tilt about *a* and *b* axes. (c), (d) Schematics of the interfacial coupling of oxygen octahedra across an interface between two perovskite oxides. (c) The octahedra of SRO are kept tilted when grown on tilted perovskite substrate, while (d) the octahedra rotations are suppressed when deposited on untilted perovskite such as STO. The octahedra of SRO film are in blue, while the octahedra of the substrates are in pink.

The magnetic anisotropy of the SRO monoclinic and tetragonal phases can also be investigated by the electrical transport measurements under the application of magnetic field. To investigate the magnetic anisotropy of both monoclinic and tetragonal phases, we measured the angle-dependent MR under a 4 T magnetic field applied in the (100) plane as well as in the (010) plane. The currents were kept normal to the magnetic field all throughout the measurement. The field angle θ is defined as shown in the inset of each figure. For SRO material that has strong magnetic anisotropy, the magnetic moment does not follow the change of direction of the applied

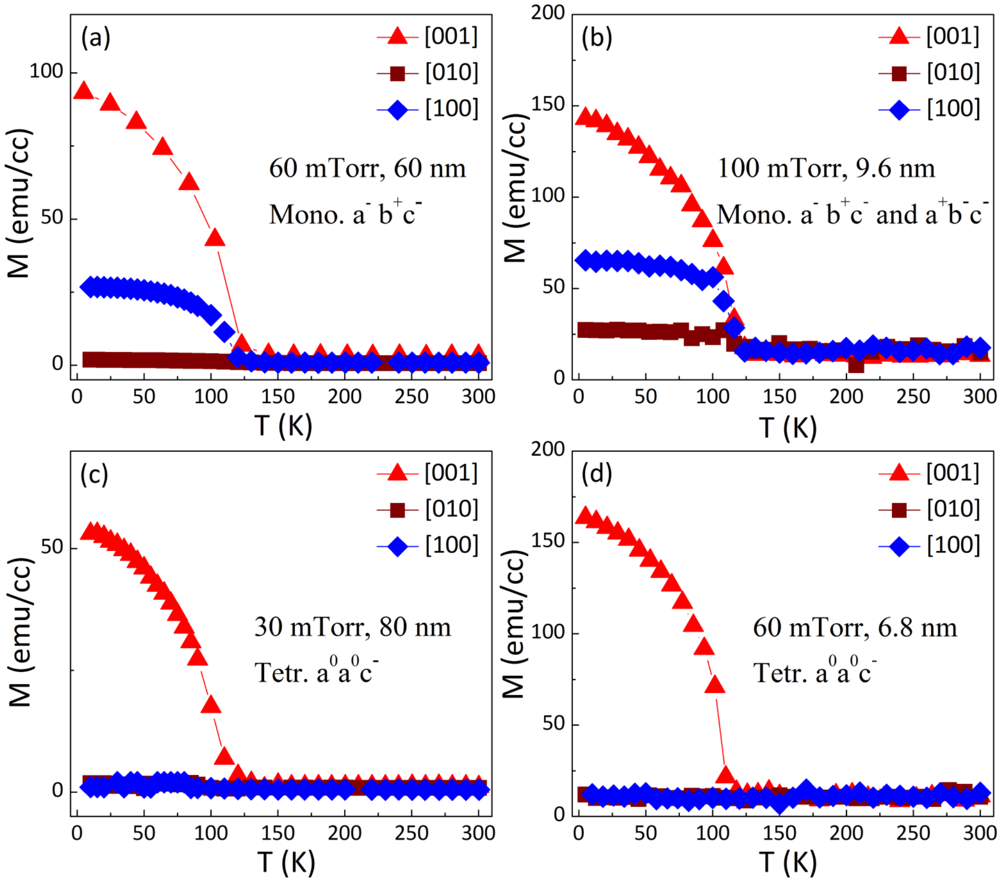

FIG. 7. (Color online) Temperature dependence of magnetization curve taken after field-cooled from room temperature with the application of a 100 Oe magnetic field. (a) and (b) show the in-plane magnetic anisotropy for monoclinic SRO films, while (c) and (d) exhibit the perpendicular uniaxial anisotropy, which matches well with the structural symmetry of octahedral tilts.

magnetic field. The magnetization reversal immediately takes place once the angle between the field and the easy axis exceeds 90°, resulting in jumps or peaks in MR.

Figures 8(a) and 8(b) present the field angle dependence of MR for the 60 nm monoclinic film with the application of magnetic field in the (100) and (010) planes, respectively. Clear peaks are observed in Fig. 8(a) with the hysteresis in the clockwise and anticlockwise field rotations after every 180° in θ. Note that the center of the hysteresis are seen at $\pm 90°$ in θ, revealing that the moment is along the [001] direction with $\theta = 0°$. This indicates that the magnetic moment of the monoclinic film is confined in the (010) plane, which is consistent with the magnetization measurement [Figs. 7(a) and 7(b)] that the moment is almost zero along [010] axis. We also measured the angle-dependent MR by rotating the magnetic field in the (010) plane in order to determine the direction of the magnetic easy axis. In Fig. 8(b), we see clear jumps in MR due to the field-induced magnetization reversal at every 180° in θ, revealing the uniaxial magnetic anisotropy of the monoclinic film. Hysteresis is observed with the jumps in the clockwise and anticlockwise rotations of the magnetic field, revealing the strong magnetic anisotropy of the film. The center of the hysteresis in the clockwise and anticlockwise field rotations lies at 60° and 120° in θ, implying that the hard axis lies at 60° and 120° away from the surface normal, consistent with the earlier work[46] on the magnetic anisotropy of SRO films. This indicates that the monoclinic film has the uniaxial magnetic anisotropy with the easy axis ~30° away from the out-of-plane direction [001] towards the [100] direction. The easy axis angle α is given in the inset of Fig. 8(b) and is close to the previously reported value of 27°.[47] The significant difference between the MR measurement in the (100) and (010) planes indicates that the monoclinic phase displays an in-plane uniaxial magnetic anisotropy, which is consistent with the magnetization measurements and could be attributed to the different rotation pattern of octahedra. For the monoclinic 100 mTorr, 9.6 nm film, there are two sets of hysteresis with sharp jumps as shown in Fig. 8(e), the centers of which are indicated by black and blue dashes, respectively. This is due to the coexistence of domains with $a^-b^+c^-$ and $a^+b^-c^-$ tilts, as is demonstrated in Fig. 3(c).

For the tetragonal film in which both [100] and [010] are hard axes, we are able to determine the easy axis by applying the magnetic field either in (100) or (010) plane. Figure 8(c) presents the field angle dependence of MR under a 4 T magnetic field in the (100) plane for the 6.8-nm-thick tetragonal film deposited in 60 mTorr oxygen. Magnetoresistance shows peaks in the clockwise and anticlockwise field rotations due to the field-induced magnetization reversal. From the center angle of the peaks in the clockwise and anticlockwise field rotations which lies at $\pm 90°$ in θ, the easy axis angle α is determined to be at 0° in θ. In addition to this measurement with the field

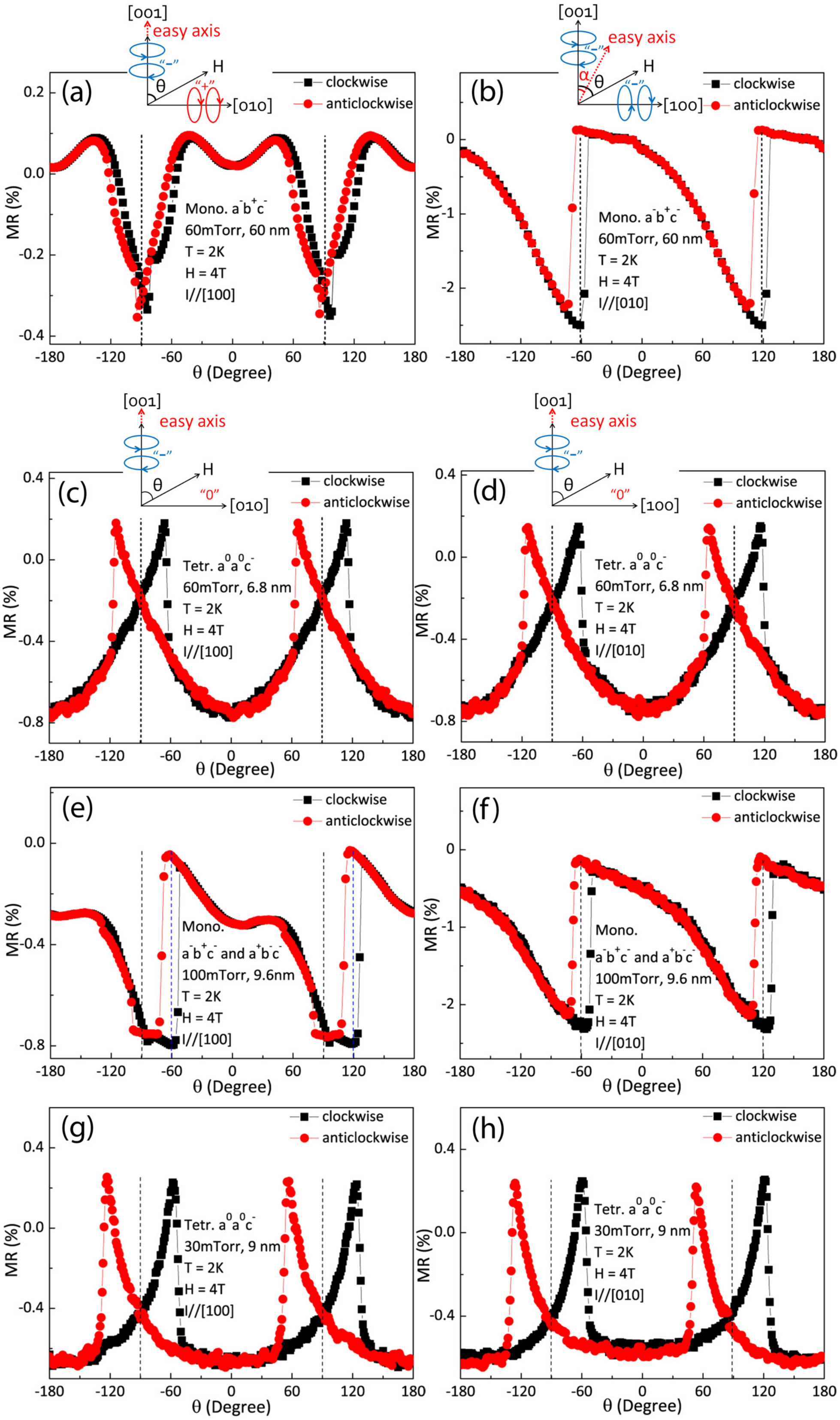

FIG. 8. (Color online) Magnetic field angle θ dependence of magnetoresistance (MR) for the (a), (b) 60 nm film deposited in 60 mTorr oxygen, (c), (d) 6.8 nm film deposited in 60 mTorr oxygen, (e), (f) 9.6 nm film deposited in 100 mTorr oxygen, and (g), (h) 9 nm film deposited in 30 mTorr oxygen. The currents were kept perpendicular to the magnetic field all through the measurement. In (a), (c), (e), and (f), the currents were applied along [100] direction and magnetic field were rotated in the (100) plane. In (b), (d), (f), and (h), the currents were applied along [010] direction and the magnetic fields were rotated in the (010) plane. The definition of the field angle is shown.

applied in (100) plane, we also performed the angle-dependent MR measurement by applying the field in (010) plane. In contrast to the monoclinic film, the 6.8-nm-thick tetragonal film displays identical angle-dependent MR curves with the magnetic field rotated in the (100) and (010) planes [see Figs. 8(c) and 8(d)]. This identity is in agreement with the superposed magnetization curves along [100] and [010] directions, further confirming the same octahedral tilts along the two orthogonal in-plane axes. Similar angle-dependent MR curves are observed in Figs. 8(g) and 8(h) for the 30 mTorr, 9 nm film that exhibits tetragonal structure.

The field angle dependence of MR for other samples was also investigated. The results show that the monoclinic film has the easy axis 30° tilted from the film normal direction, while the tetragonal film exhibits the easy axis along the out-of-plane direction. This indicates that the octahedral rotations play a significantly role in determining the structural symmetry and thus the magnetic anisotropy in SRO film. One possible mechanism responsible for the connection between the octahedral rotations and magnetic anisotropy is the orbital overlap. In SRO, the magnetic coupling depends on the overlap between the Ru 4*d* orbitals. Octahedral rotations of out-of-phase type or in-phase type have different effects on the orbital overlap. It has been supposed that the overlap between Ru 4*d* orbitals will be enhanced along the direction where the octahedra are rotated out-of-phase, which may result in a larger bandwidth along that particular direction and thus make it magnetic easier.[37] This would explain the easy axis that lies between [100] and [001] in monoclinic phase, along which the octahedra are rotated out of phase; it would also account for the perpendicular uniaxial magnetic anisotropy of the tetragonal phase in which the out-of-phase octahedral rotation is along surface normal. This hypothesis however warrants further study.

IV. CONCLUSIONS

We report the control over octahedral tilts in SRO film on (001) STO substrate by coherently controlling the oxygen vacancies and interfacial coupling. The octahedral tilt system, which describes the rotation pattern of RuO_6 and determines the structural symmetry, is identified from half-integer reflections. It is found that monoclinic structure with $\mathbf{a}^-\mathbf{b}^+\mathbf{c}^-$ tilt is favored in stoichiometric SRO film. In contrast, for film that is oxygen deficient or relatively thin, tetragonal structure with $\mathbf{a}^0\mathbf{a}^0\mathbf{c}^-$ tilt is stabilized, driven by the oxygen vacancies in the SrO atomic plane and the interfacial coupling between film and substrate. We also investigated the physical properties of the two phases. The monoclinic film exhibits an in-plane uniaxial magnetic anisotropy with easy axis 30° away from the out-of-plane direction [001], while for tetragonal phase the easy axis is parallel to the fourfold axis pointing to the [001] direction. The in-plane uniaxial anisotropy of monoclinic film is possibly due to the opposite sign of tilts that breaks the in-plane symmetry, while for the tetragonal phase the perpendicular uniaxial magnetic anisotropy is well explained by the only sustained tilt about [001] direction. Our results demonstrate that the octahedral tilts play a critical role in determining the structural symmetry and the physical properties of SRO films. In addition, the half-integer reflection, which is a straightforward and effective way in determining the octahedral tilt system, is particularly an appealing approach to investigate the tilting of the octahedra in perovskite materials.

ACKNOWLEDGMENTS

The authors are grateful for the technical support received at BL14B1 (diffractometry) beam line of Shanghai Synchrotron Radiation Facility (SSRF) for the data collection under Project No. j12sr0138. P.Y. thanks the support from SSLS via NUS Core Support C-380-003-003-001. The research is supported in part by the Singapore National Research Foundation under CRP Award No. NRF-CRP10-2012-02, and Ministry of Education, T11-1001-P04 and MOE2012-T2-2-031.

APPENDIX

Determination of crystallographic structure by reciprocal space mapping (RSM)

While the out-of-plane lattice constant can be calculated from the (00L) scan, the in-plane lattice constant and the unit-cell angle can only be inferred from RSM by high-resolution XRD equipped with a four-circle diffractometer.

In order to extract the structural information from RSM, we first need to know the relationship between the direct lattice and the reciprocal lattice. The three basic reciprocal lattice vectors $\vec{a}^*$, $\vec{b}^*$, and $\vec{c}^*$ are defined with respect to the primitive vectors of the real space lattice $\vec{a}$, $\vec{b}$, and $\vec{c}$:

$$\vec{a}^* = \frac{2\pi\vec{b}\times\vec{c}}{\vec{a}\,(\vec{b}\times\vec{c})},\quad \vec{b}^* = \frac{2\pi\vec{c}\times\vec{a}}{\vec{b}\,(\vec{c}\times\vec{a})},\quad \vec{c}^* = \frac{2\pi\vec{a}\times\vec{b}}{\vec{c}\,(\vec{a}\times\vec{b})}. \tag{A1}$$

Usually, the reciprocal space vectors are expressed as linear combinations of the primitive vectors $\vec{a}^*$, $\vec{b}^*$, and $\vec{c}^*$:

$$\vec{G}_{\mathrm{HKL}} = H\vec{a}^* + K\vec{b}^* + L\vec{c}^*, \tag{A2}$$

where H, K, and L are the Miller indices. For every set of parallel planes in the direct lattice specified by HKL, there is a corresponding point in the reciprocal lattice.

Consider a monoclinic structure with the unique b axis normal to the page which contains $\vec{a}$ and $\vec{c}$ vectors. A projection of this direct lattice is shown in Fig. 9(a), and its reciprocal lattice is shown in Fig. 9(b). In this case, because $\alpha = \gamma = 90°$, $\vec{b}^*$ is parallel to $\vec{b}$. The definition of the primitive reciprocal

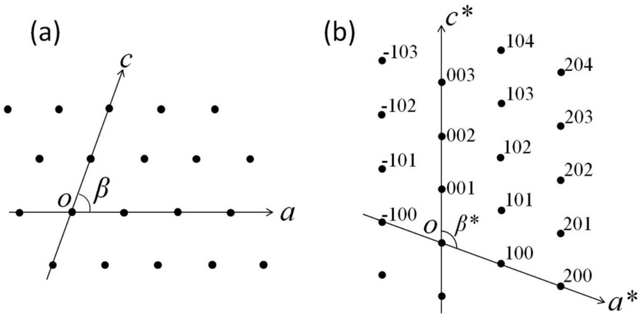

FIG. 9. The relationship between (a) a direct lattice and (b) the reciprocal lattice.

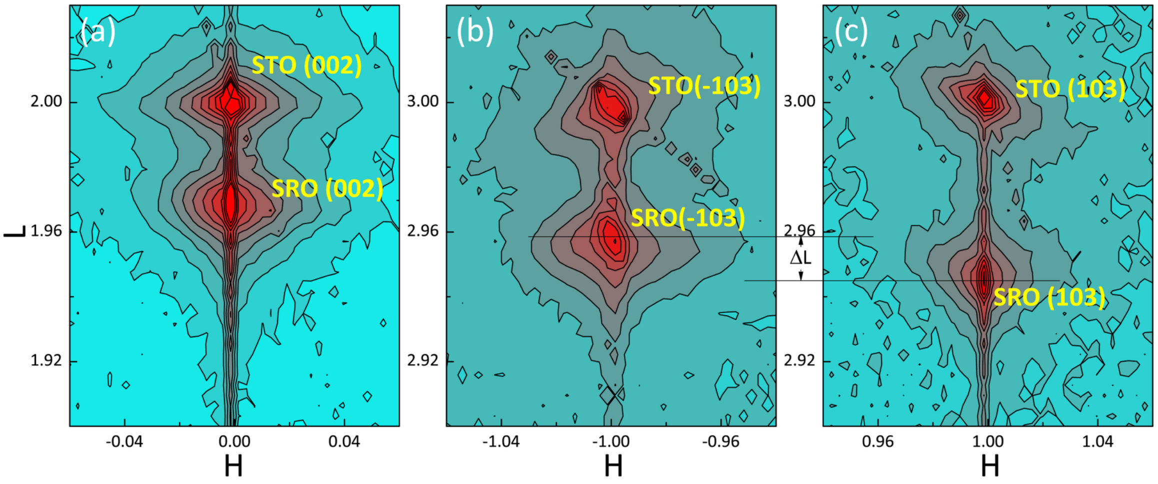

FIG. 10. (Color online) Reciprocal space mappings for the 60 nm SRO film deposited in 60 mTorr oxygen around (a) STO (002), (b) STO (−103) and (c) STO (103).

lattice vectors given in Eq. (A1) guarantees that the vector $\vec{a}^*$ is perpendicular to the b-c plane, $\vec{b}^*$ is perpendicular to the a-c plane, and $\vec{c}^*$ is perpendicular to the a-b plane. This requires that

$$\alpha + \alpha^* = 180^\circ, \quad \beta + \beta^* = 180^\circ, \quad \gamma + \gamma^* = 180^\circ. \tag{A3}$$

Note that in reciprocal space, the directions of **H**, **K**, and **L** are parallel to the reciprocal vectors $\vec{a}^*$, $\vec{b}^*$, and $\vec{c}^*$, respectively. Therefore, we can calculate the angle β^* if the positions of $(00L)$, $(H0L)$, and $(-H0L)$ points are known.

Take the 60 nm SRO film sample deposited on STO (001) substrates in 60 mTorr oxygen, for example. Before measurement, the alignment was carried out so that the coordinate of the reciprocal space is based on the ideal cubic lattice of the STO substrate. The horizontal alignment of the reciprocal lattice points of the film and substrate is shown in all the mappings, implying that the SRO film is fully strained. The **L** direction of the film can be determined from Fig. 10(a), which is parallel to that of the substrate's. The **H** direction of the film can also be determined from Figs. 10(b) and 10(c) by linking the SRO (−103) and SRO (103) points in a straight line if assuming that these two reciprocal lattice points are in the HL plane. From geometric considering [shown in Fig. 9(b)], the angle between **H** (or $\vec{a}^*$) and **L** (or $\vec{c}^*$) can be calculated by:

$$\begin{aligned}\beta^* &= 90^\circ - \arctan(\Delta L/\Delta H)\\ &= 90^\circ - \arctan\frac{2.945 - 2.958}{1-(-1)} \approx 90.4^\circ,\end{aligned} \tag{A4}$$

where ΔH and ΔL are the horizontal and vertical differences between the SRO (-103) and SRO (103) point, respectively. Here, ΔL is also clearly indicated in the Appendix, Fig. 10 The angle between a and c is thus determined to be 89.6° from Eq. (A4). Similarly, the angle α between b and c can also be determined in this way. The only difference is that the coordinates of $(0HL)$ and $(0$-$HL)$ points instead of $(H0L)$ and $(-H0L)$ points should be obtained in this situation. Although we can get some idea about the symmetry information from the two-dimensional RSM, the final structural determination can only be achieved by a set of H, K, and L scans in the three-dimensional reciprocal space, whereby the positions of reciprocal lattice points can be obtained.

---

[*] Corresponding author: msecj@nus.edu.sg

[1] J. B. Goodenough, Rep. Prog. Phys. **67**, 1915 (2004).
[2] M. B. Salamon and M. Jaime, Rev. Mod. Phys. **73**, 583 (2001).
[3] M. Imada, A. Fujimori, and Y. Tokura, Rev. Mod. Phys. **70**, 1039 (1998).
[4] L. W. Martin, Y. H. Chu, and R. Ramesh, Mater. Sci. Eng., R **68**, 89 (2010).
[5] R. J. Zeches, M. D. Rossell, J. X. Zhang, A. J. Hatt, Q. He, C.-H. Yang, A. Kumar, C. H. Wang, A. Melville, C. Adamo, G. Sheng, Y.-H. Chu, J. F. Ihlefeld, R. Erni, C. Ederer, V. Gopalan, L. Q. Chen, D. G. Schlom, N. A. Spaldin, L. W. Martin, and R. Ramesh, Science **326**, 977 (2009).
[6] W. Luo, S. J. Pennycook, and S. T. Pantelides, Phys. Rev. Lett. **101**, 247204 (2008).
[7] J. H. Haeni, P. Irvin, W. Chang, R. Uecker, P. Reiche, Y. L. Li, S. Choudhury, W. Tian, M. E. Hawley, B. Craigo, A. K. Tagantsev, X. Q. Pan, S. K. Streiffer, L. Q. Chen, S. W. Kirchoefer, J. Levy, and D. G. Schlom, Nature **430**, 758 (2004).
[8] H. Liu, P. Yang, Z. Fan, A. Kumar, K. Yao, K. P. Ong, K. Zeng, and J. Wang, Phys. Rev. B **87**, 220101 (2013).
[9] H. Liu, P. Yang, K. Yao, K. P. Ong, P. Wu, and J. Wang, Adv. Funct. Mater. **22**, 937 (2012).
[10] Z. Chen, S. Prosandeev, Z. L. Luo, W. Ren, Y. Qi, C. W. Huang, L. You, C. Gao, I. A. Kornev, T. Wu, J. Wang, P. Yang, T. Sritharan, L. Bellaiche, and L. Chen, Phys. Rev. B **84**, 094116 (2011).
[11] R. Ramesh and D. G. Schlom, MRS Bull. **33**, 1006 (2008).
[12] S. K. Streiffer and D. D. Fong, MRS Bull. **34**, 832 (2009).
[13] D. G. Schlom, L.-Q. Chen, C.-B. Eom, K. M. Rabe, S. K. Streiffer, and J.-M. Triscone, Annu. Rev. Mater. Res. **37**, 589 (2007).

[14] Y.-M. Kim, A. Kumar, A. Hatt, A. N. Morozovska, A. Tselev, M. D. Biegalski, I. Ivanov, E. A. Eliseev, S. J. Pennycook, J. M. Rondinelli, S. V. Kalinin, and A. Y. Borisevich, Adv. Mater. **25**, 2497 (2013).

[15] H. Akamatsu, Y. Kumagai, F. Oba, K. Fujita, K. Tanaka, and I. Tanaka, Adv. Funct. Mater. **23**, 1864 (2013).

[16] E. Bousquet, M. Dawber, N. Stucki, C. Lichtensteiger, P. Hermet, S. Gariglio, J.-M. Triscone, and P. Ghosez, Nature **452**, 732 (2008).

[17] J. M. Rondinelli and C. J. Fennie, Adv. Mater. **24**, 1961 (2012).

[18] V. Gopalan and D. B. Litvin, Nat. Mater. **10**, 376 (2011).

[19] N. A. Benedek and C. J. Fennie, Phys. Rev. Lett. **106**, 107204 (2011).

[20] A. M. Glazer, Acta Crystallogr. B **28**, 3384 (1972).

[21] A. M. Glazer, Acta Crystallogr. A **31**, 756 (1975).

[22] N. M. Souza-Neto, A. Y. Ramos, H. C. N. Tolentino, E. Favre-Nicolin, and L. Ranno, Phys. Rev. B **70**, 174451 (2004).

[23] R. Herger, P. R. Willmott, C. M. Schlepütz, M. Björck, S. A. Pauli, D. Martoccia, B. D. Patterson, D. Kumah, R. Clarke, Y. Yacoby, and M. Döbeli, Phys. Rev. B **77**, 085401 (2008).

[24] D. A. Muller, Nat. Mater. **8**, 263 (2009).

[25] A. Y. Borisevich, O. S. Ovchinnikov, H. J. Chang, M. P. Oxley, P. Yu, J. Seidel, E. A. Eliseev, A. N. Morozovska, R. Ramesh, S. J. Pennycook, and S. V. Kalinin, ACS Nano **4**, 6071 (2010).

[26] C. L. Jia, S. B. Mi, M. Faley, U. Poppe, J. Schubert, and K. Urban, Phys. Rev. B **79**, 081405(R) (2009).

[27] D. I. Woodward and I. M. Reaney, Acta Cryst. B **61**, 387 (2005).

[28] S. J. May, J. W. Kim, J. M. Rondinelli, E. Karapetrova, N. A. Spaldin, A. Bhattacharya, and P. J. Ryan, Phys. Rev. B **82**, 014110 (2010).

[29] R. L. Johnson-Wilke, D. S. Tinberg, C. B. Yeager, Y. Han, I. M. Reaney, I. Levin, D. D. Fong, T. T. Fister, and S. Trolier-McKinstry, Phys. Rev. B **84**, 134114 (2011).

[30] H. Rotella, U. Lüders, P. E. Janolin, V. H. Dao, D. Chateigner, R. Feyerherm, E. Dudzik, and W. Prellier, Phys. Rev. B **85**, 184101 (2012).

[31] J. He, A. Borisevich, S. V. Kalinin, S. J. Pennycook, and S. T. Pantelides, Phys. Rev. Lett. **105**, 227203 (2010).

[32] B. J. Kennedy and B. A. Hunter, Phys. Rev. B **58**, 653 (1998).

[33] D. Kan, R. Aso, H. Kurata, and Y. Shimakawa, Adv. Funct. Mater. **23**, 1129 (2013).

[34] S. H. Chang, Y. J. Chang, S. Y. Jang, D. W. Jeong, C. U. Jung, Y. J. Kim, J. S. Chung, and T. W. Noh, Phys. Rev. B **84**, 104101 (2011).

[35] A. Vailionis, W. Siemons, and G. Koster, Appl. Phys. Lett. **93**, 051909 (2008).

[36] A. Vailionis, H. Boschker, W. Siemons, E. P. Houwman, D. H. A. Blank, G. Rijnders, and G. Koster, Phys. Rev. B **83**, 064101 (2011).

[37] W. Lu, W. D. Song, K. He, J. Chai, C.-J. Sun, G.-M. Chow, and J.-S. Chen, J. Appl. Phys. **113**, 063901 (2013).

[38] W. Lu, K. He, W. Song, C.-J. Sun, G.-M. Chow, and J.-S. Chen, J. Appl. Phys. **113**, 17E125 (2013).

[39] C. S. Lue, T. H. Su, B. X. Xie, and C. Cheng, Phys. Rev. B **74**, 094101 (2006).

[40] D. O. Klenov, W. Donner, B. Foran, and S. Stemmer, Appl. Phys. Lett. **82**, 3427 (2003).

[41] W. Donner, C. Chen, M. Liu, A. J. Jacobson, Y. L. Lee, M. Gadre, and D. Morgan, Chem. Mater. **23**, 984 (2011).

[42] J. Gazquez, S. Bose, M. Sharma, M. A. Torija, S. J. Pennycook, C. Leighton, and M. Varela, APL Mat. **1**, 012105 (2013).

[43] J. M. Rondinelli and N. A. Spaldin, Phys. Rev. B **82**, 113402 (2010).

[44] S. J. May, C. R. Smith, J.-W. Kim, E. Karapetrova, A. Bhattacharya, and P. J. Ryan, Phys. Rev. B **83**, 153411 (2011).

[45] J. Y. Zhang, C. A. Jackson, S. Raghavan, J. Hwang, and S. Stemmer, Phys. Rev. B **88**, 121104(R) (2013).

[46] M. Ziese, I. Vrejoiu, and D. Hesse, Phys. Rev. B **81**, 184418 (2010).

[47] Y. Z. Yoo, O. Chmaissem, S. Kolesnik, A. Ullah, L. B. Lurio, D. E. Brown, J. Brady, B. Dabrowski, C. W. Kimball, M. Haji-Sheikh, and A. P. Genis, Appl. Phys. Lett. **89**, 124104 (2006).